1　　　Decomposition of neutron noise in a reactor into higher-order mode
2　　　components and investigation of the space and frequency dependence
3

4　　　　　　　　　　　Toshihiro Yamamoto[a,*]

5　　　　　　　　　　　Hiroki Sakamoto[b]

6
7　　*[a] Institute for Integrated Radiation and Nuclear Science, Kyoto University, 2 Asashiro-Nishi,*
8　　　　　　　*Kumatori-cho, Sennan-gun, Osaka, 590-0494, Japan*
9　　　　*[b] Radiation Dose Analysis and Evaluation Network, 4-13-14, Kokubunji-shi, Tokyo,*
10　　　　　　　　　　　　*185-0001, Japan*

11　**Abstract**

12　　　It is a well-known fact that the frequency characteristics of neutron noise induced by the

13　fluctuation of nuclear cross sections have space-dependence that departs from the point

14　kinetics behavior. In this paper, the neutron noise distribution in a two-dimensional BWR

15　core model, which is calculated by solving a two-energy group neutron noise diffusion

16　equation, is decomposed into higher-order mode components using α-mode eigenfunctions.

17　The amplitude and the phase shift of the higher-order mode components have a minor

18　dependence on the frequency, compared to the fundamental mode. Near the neutron noise

19　source, the higher-order mode components account for a major portion of the neutron noise,

20　thereby causing a minor dependence of the neutron noise on the frequency. Near the nodes

21　of the higher-order modes, the fundamental mode is dominant, and the neutron noise

22　exhibits almost the point kinetics behavior. The space dependence and the frequency

23　characteristics of the neutron noise are elucidated by examining the higher order

24　components that are decomposed from the neutron noise distribution.

25

27

*　Corresponding author. Tel:+81 72 451 2414; fax:+81 72 451 2658
　E-mail address: toshihiro.yamamoto223@gmail.com (T. Yamamoto)

1. Introduction

Neutron noise in a power reactor core, which is defined by the difference between a time-varying neutron flux and its steady state value, has the potential to provide useful information for core monitoring or diagnoses, such as abnormal vibrations of the internal core structures, or flow blockage (Seidl et al., 2015; Torres et al., 2019). For this reason, research activities on the core monitoring technique using the neutron noise have been actively pursued. In 2017, the Euratom 2016-2017 work program initiated the CORTEX project, a research and innovation action aiming to develop an innovative core monitoring technique using the fluctuations in neutron flux (Demazière et al., 2018).

Calculation tools need to be prepared to study the neutron noise behavior in a reactor core. Many kinds of computational tools for obtaining the neutron noise responses have been developed thus far. The tools mostly use diffusion theory (Pázsit and Demazière, 2010; Larsson et al., 2011; Demazière, 2011; Larsson and Demazière, 2012; Hosseini and Vosoughi, 2016; Hosseini and Vosoughi, 2018). The noise calculation method was extended to the transport theory by applying the Monte Carlo method to solve the neutron noise transport equation (Yamamoto, 2013; Yamamoto 2018) and (Rouchon et al., 2017).

In Yamamoto (2018), a neutron noise spatial distribution and its frequency characteristics were obtained by using a continuous energy Monte Carlo code that was modified to solve the neutron noise transport equation. In the paper, it was found that the frequency characteristics of the neutron noise deviate from the point kinetics behavior, and the deviation strongly depends on the location. The paper suggests that the deviation may be caused by higher order modes of the neutron noise being excited.

Very recently, Pázsit and Dykin (2018) investigated the space-dependence of the neutron noise from the viewpoint of the effect of the eigenvalue separation between the fundamental mode and the first higher order mode. Quantitative studies were performed on one-dimensional systems with different eigenvalue separations. The researchers found an

2

anomalous behavior of the neutron noise in a loosely coupled system.

The objective of the present paper is to elucidate the properties of the neutron noise in a power reactor core that were pointed out in the study by Yamamoto (2018). The neutron noise distribution and a large number of higher order modes constituting the noise distribution were obtained by solving the two-dimensional, two-energy group diffusion equations. Through this study, this paper aims to provide quantitative insight into the space-dependence and the frequency characteristics of the neutron noise in a reactor core.

2. Theory of higher order mode in neutron noise

2.1 Neutron noise equation in the diffusion theory

This section presents a fundamental theory on the diffusion equation of the neutron noise in the frequency domain. The equation has been derived and presented in many previously published literature reports (e.g., Behringer et al., 1979; Larsson et al., 2011; Demazière, 2011; Larsson and Demazière, 2012). The transport equation describing the neutron noise propagation has been introduced recently in (Yamamoto, 2013; Rouchon et al., 2017; Yamamoto 2018). The transport theory can provide an almost exact solution for the neutron noise propagation, and the analysis of this paper should have been based on the transport theory. However, attaining the purpose of this paper requires a higher-order mode analysis of neutron noise, which would be an extremely difficult task for the transport theory, even if a state-of-art technique were introduced. Therefore, throughout this paper, the discussion of the neutron noise is based on the diffusion theory instead of the transport theory. Using the diffusion theory would lend itself to the purpose of this paper.

The neutron noise in the time domain is defined as the difference between a time-varying neutron flux and its mean value:

$$\delta\phi_g(\boldsymbol{r}, t) \equiv \phi_g(\boldsymbol{r}, t) - \phi_{0g}(\boldsymbol{r}), \tag{1}$$

where $\phi_g(\boldsymbol{r}, t) =$ the neutron flux of the gth energy-group at position $\boldsymbol{r}$ and time t. The subscript "0" denotes the mean value of the time-varying quantity. This neutron noise is

assumed to be caused by the time variation of the macroscopic cross sections. The time variation of the macroscopic cross sections is as follows:

$$\delta \Sigma_{xg}(\boldsymbol{r},t) \equiv \Sigma_{xg}(\boldsymbol{r},t) - \Sigma_{x0g}(\boldsymbol{r}), \tag{2}$$

where x denotes a reaction type (absorption, fission, scattering, etc.). To convert the time variation of the cross section to the frequency domain, the time variation of the macroscopic cross section of the reaction x is Fourier transformed as follows:

$$\delta \Sigma_{xg}(\boldsymbol{r},\omega) \equiv \int_{-\infty}^{+\infty} \delta \Sigma_{xg}(\boldsymbol{r},t)\, e^{-i\omega t} dt, \tag{3}$$

where ω = the angular frequency, $i = \sqrt{-1}$. In the same manner, the neutron noise in the frequency domain, $\phi_g(\boldsymbol{r},\omega)$, is obtained by Fourier transforming the neutron noise in the time domain as follows:

$$\delta \phi_g(\boldsymbol{r},\omega) \equiv \int_{-\infty}^{+\infty} \delta \phi_g(\boldsymbol{r},t)\, e^{-i\omega t} dt. \tag{4}$$

The neutron noise diffusion equation in the frequency domain is derived from the time-dependent neutron diffusion equation and an equation for the delayed neutron precursor density using a linear approximation and a Fourier transformation. The equation finally obtained is shown below (Pázsit and Demazière, 2010):

$$
\begin{aligned}
&-\nabla D_g \cdot \nabla \delta \phi_g(\boldsymbol{r},\omega) + \Sigma_{a0g}(\boldsymbol{r})\delta \phi_g(\boldsymbol{r},\omega) + \sum_{\substack{g'=1 \\ g \neq g'}}^{G} \Sigma_{s0}^{g \to g'}(\boldsymbol{r})\delta \phi_g(\boldsymbol{r},\omega) \\
&= \frac{\chi_g}{k_{eff}}\left(1 - \frac{i\omega\beta}{i\omega + \lambda}\right)\sum_{g'=1}^{G} \nu\Sigma_{f0g'}(\boldsymbol{r})\delta \phi_{g'}(\boldsymbol{r},\omega) + \sum_{\substack{g'=1 \\ g \neq g'}}^{G} \Sigma_{s0}^{g' \to g}(\boldsymbol{r})\delta \phi_{g'}(\boldsymbol{r},\omega) \\
&\quad - \frac{i\omega}{v_g}\delta \phi_g(\boldsymbol{r},\omega) + S_g(\boldsymbol{r},\omega),
\end{aligned}
\tag{5}
$$

where λ = the time decay constant of the delayed neutron precursors, S = the noise source, and other notations are standard in the nuclear engineering. For simplicity, delayed neutrons are collapsed to one group and the difference of the neutron spectra between the prompt and delayed fission neutrons is neglected.

The noise source in the frequency domain, $S_g(\boldsymbol{r},\omega)$, is defined by the following:

4

$$S_g(\boldsymbol{r}, \omega) \equiv -\delta\Sigma_{ag}(\boldsymbol{r}, \omega)\phi_{0g}(\boldsymbol{r}) - \sum_{\substack{g'=1 \\ g \neq g'}}^{G} \delta\Sigma_s^{g \to g'}(\boldsymbol{r}, \omega)\phi_{0g}(\boldsymbol{r})$$

$$+ \sum_{\substack{g'=1 \\ g \neq g'}}^{G} \delta\Sigma_s^{g' \to g}(\boldsymbol{r}, \omega)\phi_{0g'}(\boldsymbol{r}) \qquad (6)$$

$$+ \frac{\chi_g}{k_{eff}}\left(1 - \frac{i\omega\beta}{i\omega + \lambda}\right)\sum_{g'=1}^{G} \delta\nu\Sigma_{fg'}(\boldsymbol{r}, \omega)\phi_{0g'}(\boldsymbol{r})$$

1   Eq. (5) is a commonly used multigroup diffusion equation for the neutron noise propagation

2   in a critical state reactor core. The method for solving Eq. (5) was already established and

3   published in many papers. Although Eq. (5) contains complex-valued variables, the

4   conventional computational techniques for solving the real-valued fixed source problem are

5   available for the diffusion equation of the complex-valued neutron noise.

6

7   **2.2 Decomposition of neutron noise into higher-order modes**

8   The purpose of this study is to investigate the effect of the higher-order modes in the

9   neutron noise. This section describes how to express the neutron noise, $\delta\phi_g(\boldsymbol{r}, \omega)$, by the

10   sum of the higher-order mode components. The method to decompose a neutron flux

11   distribution into the sum of eigenfunction components is already shown in many papers (e.g.,

12   Yamamoto et al., 2003; Verdú and Ginestar, 2014; Abrate et al., 2019). Yamamoto et al.

13   (2003) used the γ–mode eigenfunctions in an exponential experiment to decompose a

14   neutron flux distribution. This paper follows the method in Yamamoto et al. (2003) to

15   decompose the neutron noise distribution. The neutron noise, $\delta\phi_g(\boldsymbol{r}, \omega)$, can be expanded

16   by an arbitrary orthogonal function such as the lambda mode eigenfunction and the alpha

17   mode eigenfunction. According to Verdú and Ginestar (2014), both the lambda and alpha

18   modes yield a very similar results for a critical or nearly critical reactor. The present study

19   deals with the property of neutron noise in a critical reactor. Thus, both modes can be

20   available for this study. Then, this study chooses the α-mode eigenfunction as an orthogonal

21   function to expand the neutron noise. The equations in this section are essentially the same

5

as those in (Yamamoto et al., 2003) where the γ–mode eigenfunctions are used for decomposition. Using the mth order α-mode eigenfunctions, ψ_g^m, the neutron noise is expanded as follows:

$$\delta\phi_g(\mathbf{r}, \omega) = \sum_{m=0}^{\infty} a_m(\omega)\psi_g^m(\mathbf{r}), \tag{7}$$

where $a_m(\omega)$ is the frequency-dependent expansion coefficient. The ψ_g^m is the mth order eigenfunction of the α-mode eigenvalue equation as follows:

$$\mathbf{M}_g(\mathbf{r})\psi_g^m(\mathbf{r}) = \frac{\alpha_m}{v_g}\psi_g^m(\mathbf{r}), \tag{8}$$

where

$$\mathbf{M}_g(\mathbf{r})\psi_g^m(\mathbf{r}) \equiv -\nabla D_g(\mathbf{r}) \cdot \nabla\psi_g^m(\mathbf{r}) + \Sigma_{a0g}(\mathbf{r})\psi_g^m(\mathbf{r}) + \sum_{\substack{g'=1 \\ g \neq g'}}^{G} \Sigma_{s0}^{g\rightarrow g'}(\mathbf{r})\psi_g^m(\mathbf{r})$$
$$- \chi_g \sum_{g'=1}^{G} \nu\Sigma_{f0g'}(\mathbf{r})\psi_{g'}^m(\mathbf{r}) - \sum_{\substack{g'=1 \\ g \neq g'}}^{G} \Sigma_{s0}^{g'\rightarrow g}(\mathbf{r})\psi_{g'}^m(\mathbf{r}). \tag{9}$$

Note that ν in Eq. (9) is the number of prompt and delayed neutrons per fission. Thus, the α-mode in this paper is different from the usual α-mode where only the prompt neutrons are considered and the delayed neutrons are neglected. In this α-mode, the α-eigenvalue is zero when the reactor is critical, which means that the fundamental mode of the α-mode is equivalent to the λ-mode in a critical state reactor.

The adjoint equation to Eq. (8) is defined as follows:

$$\mathbf{M}_g^*(\mathbf{r})\Psi_g^m(\mathbf{r}) = \frac{\alpha_m}{v_g}\Psi_g^m(\mathbf{r}), \tag{10}$$

where

$$\mathbf{M}_g^*(\mathbf{r})\Psi_g^m(\mathbf{r}) \equiv -\nabla D_g(\mathbf{r}) \cdot \nabla\Psi_g^m(\mathbf{r}) + \Sigma_{a0g}(\mathbf{r})\Psi_g^m(\mathbf{r}) + \sum_{\substack{g'=1 \\ g \neq g'}}^{G} \Sigma_{s0}^{g'\rightarrow g}(\mathbf{r})\Psi_g^m(\mathbf{r})$$
$$- \nu\Sigma_{f0g}(\mathbf{r}) \sum_{g'=1}^{G} \chi_{g'}\Psi_{g'}^m(\mathbf{r}) - \sum_{\substack{g'=1 \\ g \neq g'}}^{G} \Sigma_{s0}^{g\rightarrow g'}(\mathbf{r})\Psi_{g'}^m(\mathbf{r}), \tag{11}$$

and $\Psi_g^m(\mathbf{r}) =$ the mth order eigenfunction of the adjoint equation. The eigenfunctions

1 $\psi_g^m(\mathbf{r})$ and $\Psi_g^n(\mathbf{r})$ have the following relation:

$$\langle \Psi_g^n(\mathbf{r})M_g(\mathbf{r})\psi_g^m(\mathbf{r})\rangle = \langle \psi_g^m(\mathbf{r})M_g^*(\mathbf{r})\Psi_g^n(\mathbf{r})\rangle, \tag{12}$$

2 where the angle bracket denotes integration over the entire volume and summation over all

3 energy groups. Multiplying Eq. (8) by $\Psi_g^n(\mathbf{r})$, and Eq. (10) by $\psi_g^m(\mathbf{r})$, and subtracting,

4 then making use of Eq. (12) yields the following:

$$(\alpha_m - \alpha_n)\langle \psi_g^m(\mathbf{r})\frac{1}{v_g}\Psi_g^n(\mathbf{r})\rangle = 0. \tag{13}$$

5 Thus, we obtain the following orthogonality relation as follows:

$$\langle \psi_g^m(\mathbf{r})\frac{1}{v_g}\Psi_g^n(\mathbf{r})\rangle = 0 \quad \text{for } m \neq n \text{ and } \alpha_m \neq \alpha_n, \tag{14}$$

$$\langle \psi_g^m(\mathbf{r})\frac{1}{v_g}\Psi_g^n(\mathbf{r})\rangle \neq 0 \quad \text{for } m = n. \tag{15}$$

6 Multiplying both sides of Eq. (7) by $\Psi_g^n(\mathbf{r})/v_g$, integrating them over the whole phase

7 space, and using the orthogonality relation yield the frequency-dependent expansion

8 coefficient as follows:

$$a_m(\omega) = \frac{\langle \Psi_g^m(\mathbf{r})\frac{1}{v_g}\delta\phi_g(\mathbf{r},\omega)\rangle}{\langle \Psi_g^m(\mathbf{r})\frac{1}{v_g}\psi_g^m(\mathbf{r})\rangle}. \tag{16}$$

9 Because the neutron noise, $\delta\phi_g(\mathbf{r},\omega)$, is a complex value, $a_m(\omega)$ is also a complex value.

10 The frequency dependence of each mode is represented by the expansion coefficient,

11 $a_m(\omega)$. If the eigenvalues of the *m*th and *n*th eigenfunctions are the same, that is, the two

12 eigenfunctions are degenerate, the expansion coefficients of the *m*th and *n*th eigenfunctions

13 are obtained by solving the following simultaneous equations:

$$\langle \Psi_g^n(\mathbf{r})\frac{1}{v_g}\delta\phi_g(\mathbf{r},\omega)\rangle = a_m(\omega)\langle \Psi_g^n(\mathbf{r})\frac{1}{v_g}\psi_g^m(\mathbf{r})\rangle + a_n(\omega)\langle \Psi_g^n(\mathbf{r})\frac{1}{v_g}\psi_g^n(\mathbf{r})\rangle, \tag{17}$$

$$\langle \Psi_g^m(\mathbf{r})\frac{1}{v_g}\delta\phi_g(\mathbf{r},\omega)\rangle = a_m(\omega)\langle \Psi_g^m(\mathbf{r})\frac{1}{v_g}\psi_g^m(\mathbf{r})\rangle + a_n(\omega)\langle \Psi_g^m(\mathbf{r})\frac{1}{v_g}\psi_g^n(\mathbf{r})\rangle. \tag{18}$$

14

15 **3. Numerical examples of higher order mode effect in a BWR**

16 **3.1 Specifications of the numerical test**

17   Using the method described in Sec. 2., the effect of the higher-order modes of the

1   neutron noise in a model BWR core is studied. The geometry of the BWR core is a 211 $\times$

2   211 cm two-dimensional square. It is assumed that the core is composed of only one

3   homogenized material. The two-energy group constants for the BWR whose steam content

4   is 40% are taken from (Behringer et al., 1979). The absorption cross sections in (Behringer

5   et al., 1979) include pseudo leakage in the radial direction. The group constants are modified

6   to remove the radial leakage and are adjusted in such a way that the k_{eff} of the core is exactly

7   equal to unity. The group constants and the kinetics parameters used in this paper are shown

8   in Table 1. The vacuum boundary condition ($-D_g \nabla\phi_g/\phi_g = 0.4692$) is imposed on the

9   external surfaces.

10   The diffusion equations, Eqs. (5), (8), and (10), are solved using the finite difference

11   method with 51×51 meshes. In the fixed source calculation to obtain the neutron noise

12   distribution, a real-valued noise source is placed at an off-center position, which is 81.9 cm

13   remote from the core center, as shown in Fig. 1. This source position is chosen to excite the

14   asymmetric higher-order modes. It is assumed that the noise source is in only the thermal

15   energy group. The neutron noises are evaluated along the diagonal line, as shown in Fig. 1.

16   A value in parenthesis in Fig. 1 denotes the distance from the source position.

17   The α-mode eigenvalue problems for Eqs. (8) and (10) are solved using the

18   RHEINGOLD code that was developed by one of the authors (Yamamoto et al., 2003). The

19   RHEINGOLD code solves a matrix eigenvalue equation directly with the double QR

20   method to obtain higher-order eigenvalues and eigenfunctions. The matrix eigenvalue

21   equation is derived from the difference equation for Eqs. (8) or (10). The dimensions of the

22   matrix and the number of the higher-order modes calculated by the code are the number of

23   mesh points times the number of energy groups (51×51×2=5,202).

24   [Table 1][Fig. 1]

25   **3.2 Frequency dependence of neutron noise and each mode**

26   Using the RHEINGOLD code, the higher-order mode fluxes and eigenvalues are

27   calculated up to the 5,202th mode. The schematic drawings of the higher-order mode fluxes

1 up to the 9th mode are shown in Fig. 2, along with the corresponding α-eigenvalues.

2 [Fig. 2]

3   The neutron noise is evaluated at the five locations as shown in Fig. 1. The amplitude of

4 the thermal neutron noise, $|\delta\phi_2(\boldsymbol{r}, \omega)|$, vs. the frequency is shown in Fig. 3. The amplitude

5 of the point kinetics is also shown in Fig. 3. The point kinetics is given by the following:

$$G_0(\omega) = \frac{1}{i\omega\left(\Lambda + \dfrac{\beta}{\lambda + i\omega}\right)},$$ (19)

6 where the neutron generation time $\Lambda = 4.353 \times 10^{-5}$ s. The neutron generation time is

7 obtained by the perturbation theory using the forward and adjoint fluxes. The amplitude at

8 each position is normalized to have the same value at 1 Hz. Fig. 4 shows the phase shift of

9 the thermal neutron noise as a function of frequency at the same locations as in Fig. 3. As

10 remarked in (Yamamoto, 2018), Figs. 3 and 4 show that the amplitude and the phase shift

11 near the noise source (the position A) exhibit a weak dependence on frequency. At position

12 C, which is the core center, the frequency dependence of the amplitude and the phase shift

13 are similar to the point kinetics. This is partly because the asymmetric higher-order mode

14 noises are not excited at the core center. This tendency is discussed in detail below.

15 [Fig. 3][Fig. 4]

16   The frequency-dependent expansion coefficients are calculated using Eq. (16). The

17 amplitude and the phase shift of the coefficient, $a_m(\omega)$, for $m = 0$ (fundamental), 1, 3, 7,

18 10, and 90 are shown in Figs. 5 and 6, respectively. As seen in Figs. 1 and 2, the second

19 order mode is not excited, because the noise source is located at the node of the mode. That

20 is why the second order mode is not shown in Figs. 5 and 6. The expansion coefficient of the

21 fundamental mode, $a_0(\omega)$, is nearly the same as the point kinetics in terms of both the

22 amplitude and the phase shift. The expansion coefficients of the higher-order modes,

23 $a_m(\omega)$, for $m \geq 1$, are almost independent of the frequency in the lower frequency region.

24 Far beyond the plateau frequency region (0.01 ~ 25 Hz), the higher order modes exhibit

25 significant dependency on the frequency. The higher the mode order becomes, the smaller

the dependence on the frequency becomes. Thus, Figs. 3, 4, 5, and 6 suggest that the higher

order modes, which have smaller dependence on the frequency, comprise a major part of the

neutron noise near the noise source compared to the fundamental mode. Next, the neutron

noise is decomposed into the mode components. The frequency is divided into three regions:

below, above, and within the plateau frequency region. The property of the mode

components in each frequency region is discussed below.

[Fig. 5][Fig. 6]

3.3 Higher-order modes within the plateau frequency region (1 Hz)

The real part of the thermal neutron noise (Re[φs]), the fundamental mode (Re[φ0]),

the first-order mode (Re[φ1]), and the third-order mode (Re[φ3]) along the diagonal line

are shown in Fig. 7. The imaginary part of the thermal neutron noise (Im[φs]) and the

fundamental mode (Im[φ0]) are also shown in Fig. 7. Around the source position (70 cm

from the corner, near the position A), the real part of the thermal neutron noise is much

larger than the fundamental mode. This means that the higher-order modes account for a

significant portion of the neutron noise around the noise source. On the other hand, the

fundamental mode is dominant around the core center, where many of the higher-order

modes have their nodes. The fundamental mode appears to be dominant at a farther position

from the core center. However, this is due to the cancellation of the positive and negative

higher-order modes, because one can see that the first- and the third-order modes cancel out

each other beyond the core center. The imaginary part of the neutron noise is mostly

dominated by the fundamental mode, and the effect of the higher-order modes is negligibly

small.

[Fig. 7]

Summing $a_m(\omega)\psi_g^m(\boldsymbol{r})$ up to m = 2,601 (= 51×51) mostly converges to the neutron

noise calculated by solving Eq. (5). Here, the convergence situation is studied by changing

the upper limit of the higher-order mode, *M* as follows:

$$\delta\phi_{g,M}(\boldsymbol{r},\omega) = \sum_{m=0}^{M} a_m(\omega)\psi_g^m(\boldsymbol{r}). \tag{20}$$

1   Figs. 8, 9, and 10 show $\delta\phi_{2,M}(\boldsymbol{r},\omega)$ as a function of M at the positions A, C, and E,

2   respectively. The position A is very near the noise source, position C is at the core center,

3   and position E is located at the opposite side of the noise source with respect to the core

4   center. Fig. 8 indicates that summing <mark>half of</mark> all higher-order modes is required to obtain the

5   converged neutron noise near the noise source. Around the core center, the fundamental

6   mode and the next mode account for a major portion of the converged neutron noise, as seen

7   in Fig. 9. The higher order modes have a minor influence on the neutron noise around the

8   core center. Fig. 10 indicates that beyond the core center many positive and negative

9   higher-order modes cancel out each other until the convergence is attained. In conclusion, a

10   large number of higher-order modes have to be summed to reconstruct the converged

11   neutron noise, except near the core center. With regards to the imaginary part, the effect of

12   the higher order modes are negligible, regardless of the location.

13   [Fig. 8][Fig. 9][Fig. 10]

14   **3.4 Higher-order modes below the plateau frequency region (0.01 Hz)**

15   The real part of the thermal neutron noise (Re[φs]), the fundamental mode (Re[φ0]),

16   the first-order mode (Re[φ1]), and the third-order mode (Re[φ3]) along the diagonal line

17   are shown in Fig. 11 for the frequency 0.01 Hz. The characteristics of the neutron noise in

18   frequency 0.01 Hz are essentially the same as in the plateau frequency region (1 Hz), except

19   that the imaginary part of the neutron noise is equivalent in magnitude to the real part.

20   [Fig. 11]

21   **3.5 Higher-order modes above the plateau frequency region (100 Hz)**

22   The real part of the thermal neutron noise (Re[φs]), the fundamental mode (Re[φ0]),

23   the first-order mode (Re[φ1]), and the third-order mode (Re[φ3]) along the diagonal line

24   are shown in Fig. 12 for the frequency 100 Hz. The imaginary parts corresponding to the

25   real parts in Fig. 12 are shown in Fig. 13. The situation in this high-frequency region is quite

26   different from the first two cases (0.01 Hz and 1 Hz). The fundamental mode (Re[φ0]) is

smaller than $\mathrm{Re}[\varphi 1]$ and $\mathrm{Re}[\varphi 3]$, except around the core center. That is, the neutron noise is dominated by higher-order modes in most parts of the core. This can be suggested by the fact that the amplitude of the fundamental mode decreases with the frequency beyond the plateau frequency region, while those of the higher-order modes are kept mostly constant, as shown in Fig. 5. The imaginary part of the neutron noise has a peak around the noise source. This means that some higher-order modes are significantly excited, even in the imaginary part, unlike in the plateau and low-frequency regions.

[Fig. 12][Fig. 13]

The space-dependent neutron noise has a unique property in the higher frequency range. At the points that are far from the noise source (e.g., the positions C, D, and E), the absolute value of the phase shift, $|\angle\delta\phi_2(\boldsymbol{r},\omega)|$, exceeds 90 degrees as can be seen in Figs. 12 and 13. The phase shift, $|\angle\delta\phi_2(\boldsymbol{r},\omega)|$, never exceeds 90 degrees in the point kinetics. Fig. 4 shows that such a situation occurs when the frequency is higher than several tens of Hz. For example, when the frequency is higher than 44 Hz, 61 Hz, and 89 Hz, $|\angle\delta\phi_2(\boldsymbol{r},\omega)|$ exceeds 90 degrees at the positions E, D, and C, respectively. As seen in Fig. 12, $\mathrm{Re}[\varphi s]$ (red curve) is negative beyond the position C where the negative higher order modes are dominant, which causes $|\angle\delta\phi_2(\boldsymbol{r},\omega)|$ to exceed 90 degrees.

Figs. 14, 15, and 16 show $\delta\phi_{2,M}(\boldsymbol{r},\omega)$ as a function of M at the positions A, C, and E, respectively. The situation of the convergence of the neutron noise in the high-frequency region is essentially the same as that in the plateau-frequency region. The exceptions are that the fundamental mode is small compared to the higher-order modes, and the imaginary parts are affected by the higher-order modes.

[Fig. 14][Fig. 15][Fig. 16]

4. Conclusions

The frequency dependence of the neutron noise are calculated at several locations in a model BWR core. The amplitude and the phase shift of the neutron noise near the noise source have a much smaller dependence on the frequency than the point kinetics behavior.

This is because the higher-order modes account for a major portion of the neutron noise near the noise source. On the other hand, around the core center where many higher-order modes have nodes, the neutron noise has frequency characteristics that are similar to the point kinetics behavior.

While the expansion coefficient of the fundamental mode is the same as the point kinetics, those of the higher-order modes have small dependence on the frequency. Hence, the fundamental mode becomes dominant below the plateau frequency region, where the fundamental mode increases with decreasing frequency and the higher-order modes remain almost constant. In contrast, the fundamental mode decreases than the higher-order modes above the plateau frequency region.

The neutron noise is decomposed into higher-order modes by using the α–mode eigenfunctions. The neutron noise around the core center can be reconstructed by summing a small number of modes. On the other hand, a large number of modes have to be summed to reconstruct the neutron noise near the noise source. At a location far from the noise source, many positive and negative higher order modes cancel out each other before reaching the convergence.

The frequency characteristics and the space dependence of the neutron noise in a model BWR core are elucidated by a higher-order mode analysis of the neutron noise. Although this study is limited within the diffusion approximation, the fundamental characteristics of the neutron noise are considered to be valid.

For more precise discussion on the higher-order mode effect, this work could be expanded to a three-dimensional geometry. In this work, the noise source is assumed to be a point source. A more realistic noise source that models some sort of anomalies (e.g., abnormal vibrations of the internal core structures, and flow blockage) in a practical power reactor should be considered. These would be considered as future work.

References

Abrate, N., Bruna, G., Dulla, S. Ravetto, P., 2019. Assessment of numerical methods for the evaluation of higher-order harmonics in diffusion theory. Ann. Nucl. Energy 128 455-470.

Behringer, K., Kosály, G., Pázsit, I., 1979. Linear response of the neutron field to a propagating perturbation of moderator density (two-group theory of boiling water reactor noise). Nucl. Sci. Eng. 72, 304-321.

Demazière, C., 2011. CORE SIM: A multi-purpose neutronic tool for research and education. Ann. Nucl. Energy 38, 2698-2718.

Demazière, C., Vinai, P., Hursin, M., Kollias, S., Herb, J., 2018. Overview of the CORTEX project. Proc. PHYSOR 2018: Reactor Physics paving the way towards more efficient systems, Cancun, Mexico, April 22-26, 2018.

Hosseini, S.A., Vosoughi, N., 2016. Development of 3D neutron noise simulator based on GFEM with unstructured tetrahedron elements. Ann. Nucl. Energy 97, 132-141.

Hosseini, S.A., Vosoughi, N., 2018. Higher order reactor noise analysis: The multigroup diffusion model. Ann. Nucl. Energy 111, 354-370.

Larsson, V., Demazière, C., Pázsit, I., Tran, H.N., 2011. Neutron noise calculations using the Analytical Nodal Method and comparisons with analytical solutions. Ann. Nucl. Energy 38, 808-816.

Larsson, V., Demazière, C., 2012. Comparison of the calculated neutron noise using finite differences and the Analytical Nodal Method. Ann. Nucl. Energy 43, 176-182.

Pázsit, I., Demazière, C., 2010. Noise techniques in nuclear systems. In: Cacuci, D.G., Ed., Handbook of Nuclear Engineering, Vol.3, 1629-1737, Springer.

14

Pázsit, I., Dykin, V., 2018. The role of the eigenvalue separation in reactor dynamics and neutron noise theory. J. Nucl. Sci. Technol. 55, 484-495.

Rouchon, A., Zoia, A., Sanchez, R., 2017. A new Monte Carlo method for neutron noise calculations in the frequency domain. Ann. Nucl. Energy 102, 465-475.

Seidl, M., Kosowski, K., Schüler, U., Belblidia, L., 2015. Review of the historic neutron noise behavior in German KWU built PWRs. Prog. Nucl. Energy 85, 668-675.

Torres, L.A., Chionis, D., Montalvo, C., Dokhane, A., Garcia-Berrocal, A., 2019. Neutron noise analysis of simulated mechanical and thermal-hydraulic perturbations in a PWR core. Ann. Nucl. Energy 126, 242-252.

Verdú, G., Ginestar, D., 2014. Modal decomposition method for BWR stability analysis using Alpha-modes. Ann. Nucl. Energy 67, 31-40.

Yamamoto, T., Miyoshi, Y., Tonoike, K., Okamoto, H., Ida, T., Aoki, S., 2003. Effect of higher-harmonic flux in exponential experiment for subcriticality measurement. J. Nucl. Sci. Technol. 40, 77-83.

Yamamoto, T., 2013. Monte Carlo method with complex-valued weights for frequency domain analyses of neutron noise. Ann. Nucl. Energy 58, 72-79.

Yamamoto, T., 2018. Implementation of a frequency-domain neutron noise analysis method in a production-level continuous energy Monte Carlo code: verification and application in a BWR. Ann. Nucl. Energy 105, 494-501.

1 <div align="center">Figure legend</div>

2 Fig. 1 The arrangement of the noise source and detection positions. The value in

3 parenthesis is the distance from the noise source.

4 Fig. 2 Schematic view of higher-order mode flux distribution up to the 9th mode and the

5 α-eigenvalues.

6 Fig. 3 Amplitude of the thermal neutron noise at the positions in Fig. 1.

7 Fig. 4 Phase shift of the thermal neutron noise at the positions in Fig. 1.

8 Fig. 5 Frequency dependence of the amplitude of expansion coefficient.

9 Fig. 6 Frequency dependence of the phase shift of expansion coefficient.

10 Fig. 7 Thermal neutron noise distribution and the decomposed higher-order mode

11 components along the diagonal line (1 Hz).

12 Fig. 8 Convergence of the thermal neutron noise at position A (near the noise source, 1 Hz).

13 Fig. 9 Convergence of the thermal neutron noise at position C (core center, 1 Hz).

14 Fig. 10 Convergence of the thermal neutron noise at position E (1 Hz).

15 Fig. 11 Thermal neutron noise distribution and the decomposed higher-order mode

16 components along the diagonal line (0.01 Hz).

17 Fig. 12 Thermal neutron noise distribution and the decomposed higher-order mode

18 components along the diagonal line (real part, 100 Hz).

19 Fig. 13 Thermal neutron noise distribution and the decomposed higher-order mode

20 components along the diagonal line (imaginary part, 100 Hz).

21 Fig. 14 Convergence of the thermal neutron noise at position A (near the noise source, 100

22 Hz).

23 Fig. 15 Convergence of the thermal neutron noise at position C (core center, 100 Hz).

24 Fig. 16 Convergence of the thermal neutron noise at position E (100 Hz).
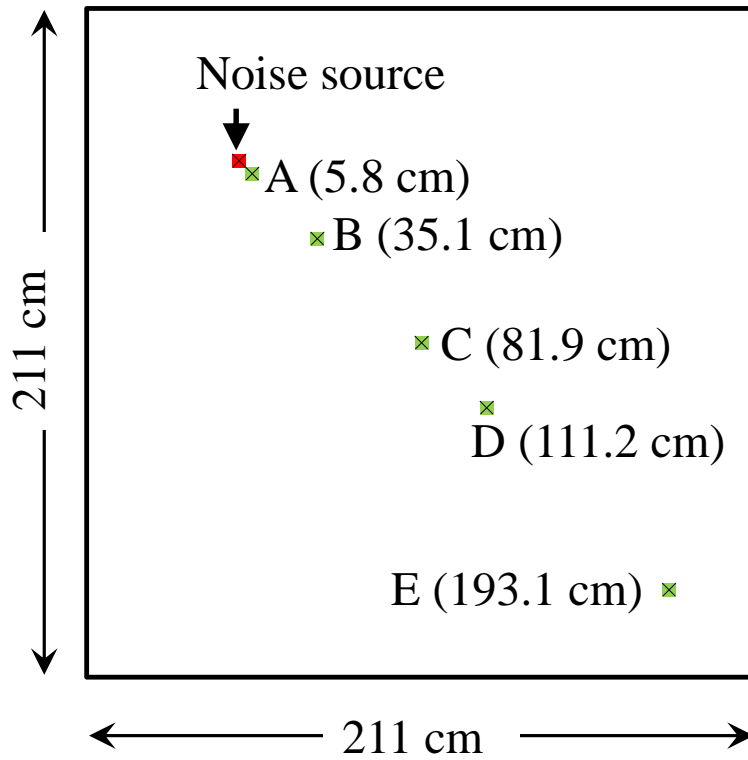
1

2

3   Fig. 1 The arrangement of the noise source and detection positions. The value in parenthesis is the

4   distance from the noise source.

5
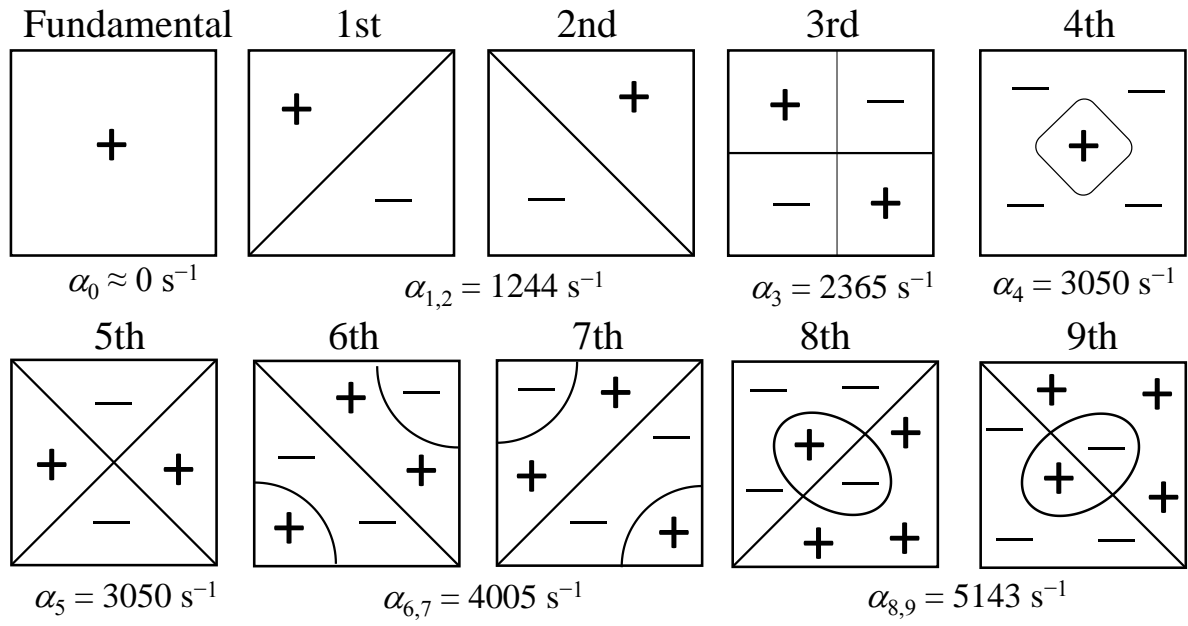
Fig. 2 Schematic view of higher-order mode flux distribution up to the 9th mode and the α-eigenvalues.
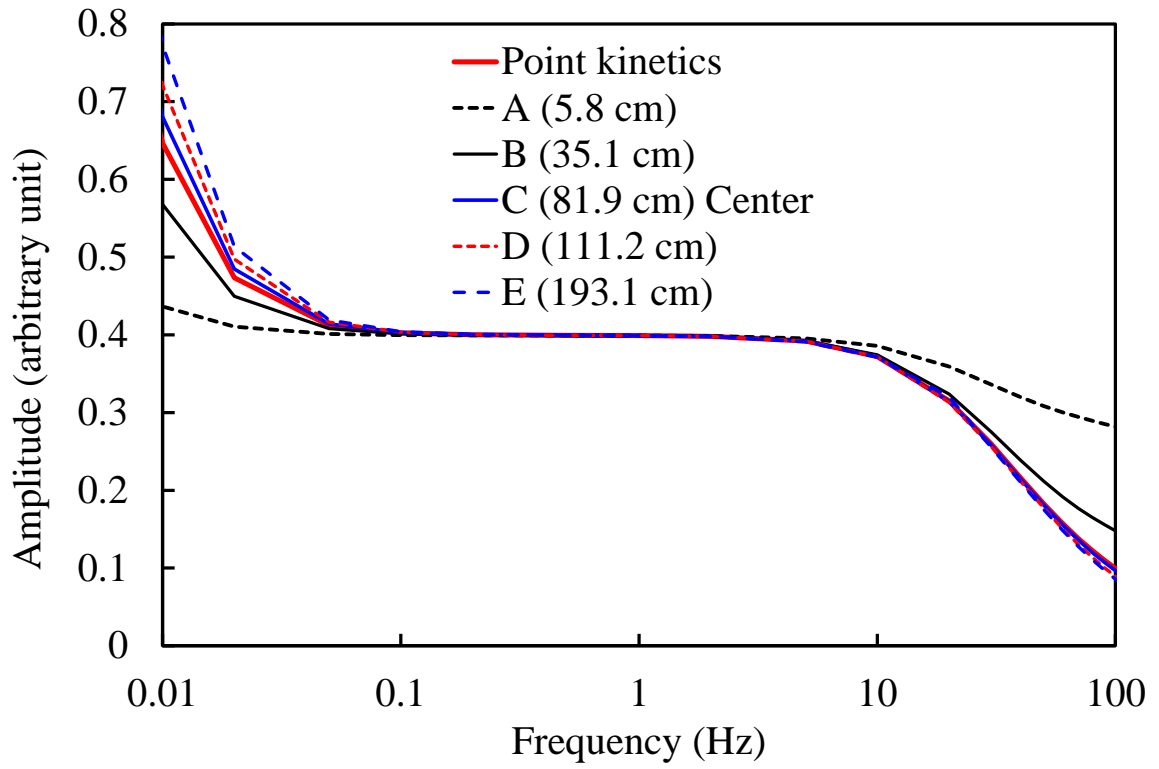
1

2

3   Fig. 3 Amplitude of the thermal neutron noise at the positions in Fig. 1.

4
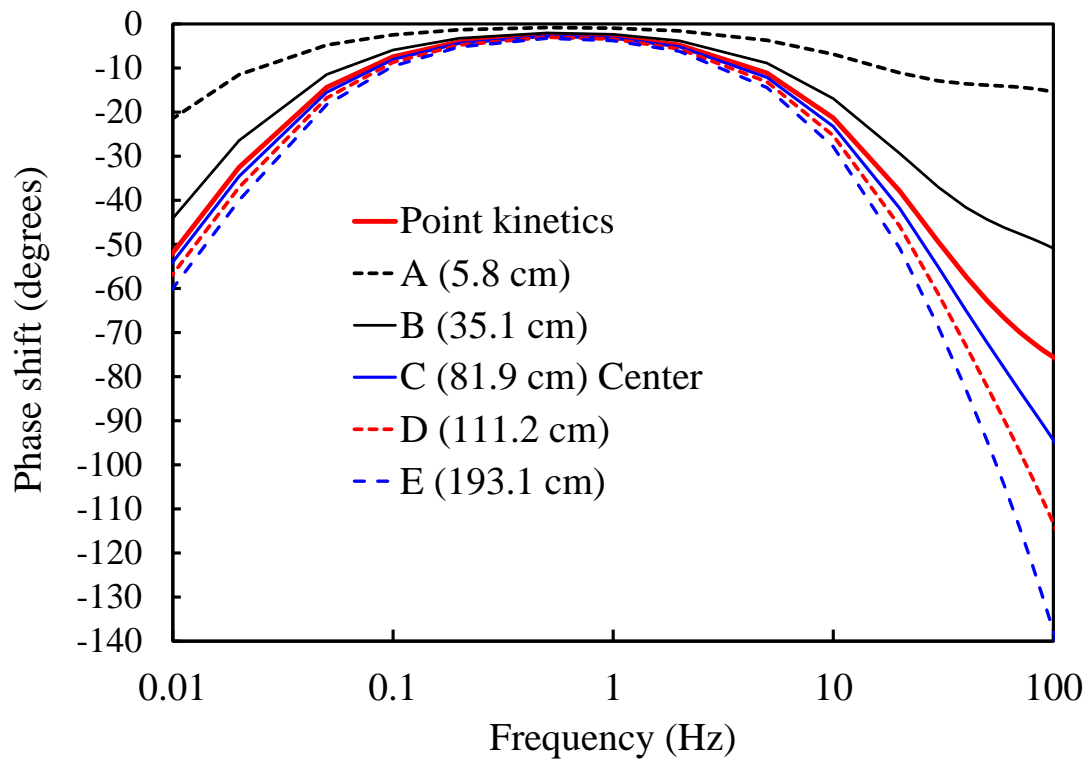
Fig. 4 Phase shift of the thermal neutron noise at the positions in Fig. 1.

1

2

3

4

5
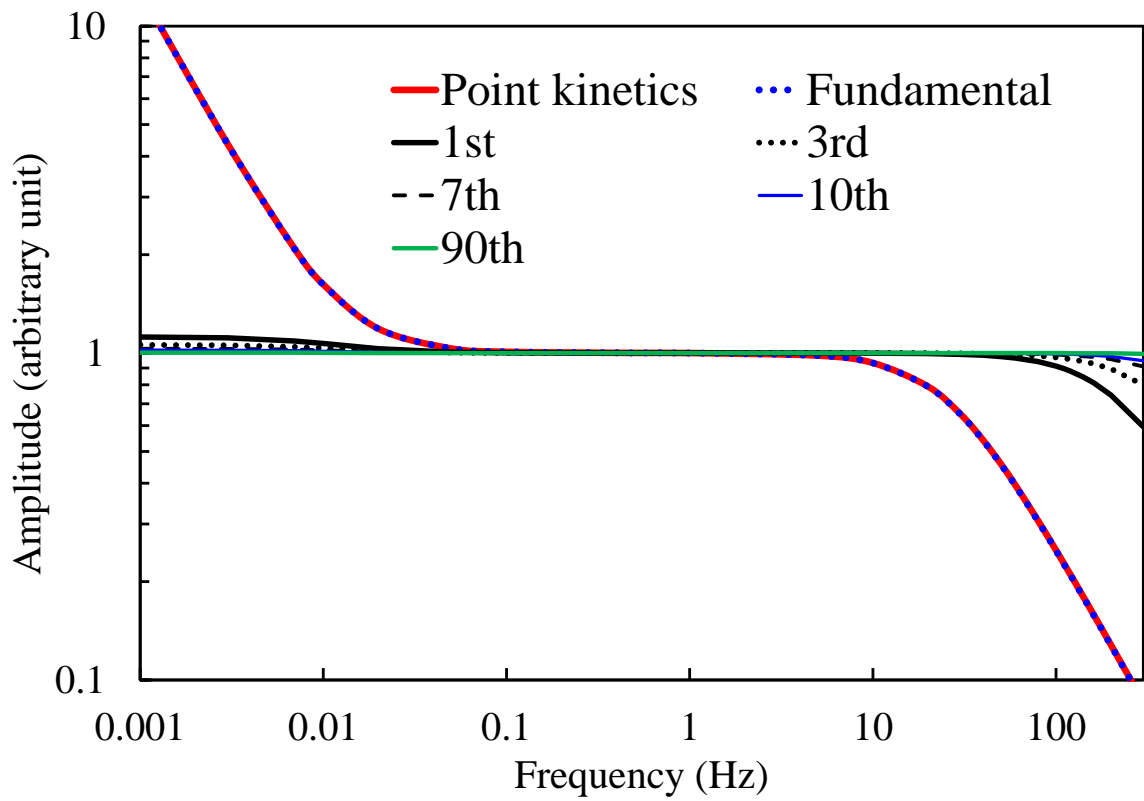
1

2

3   Fig. 5 Frequency dependence of the amplitude of expansion coefficient.

4
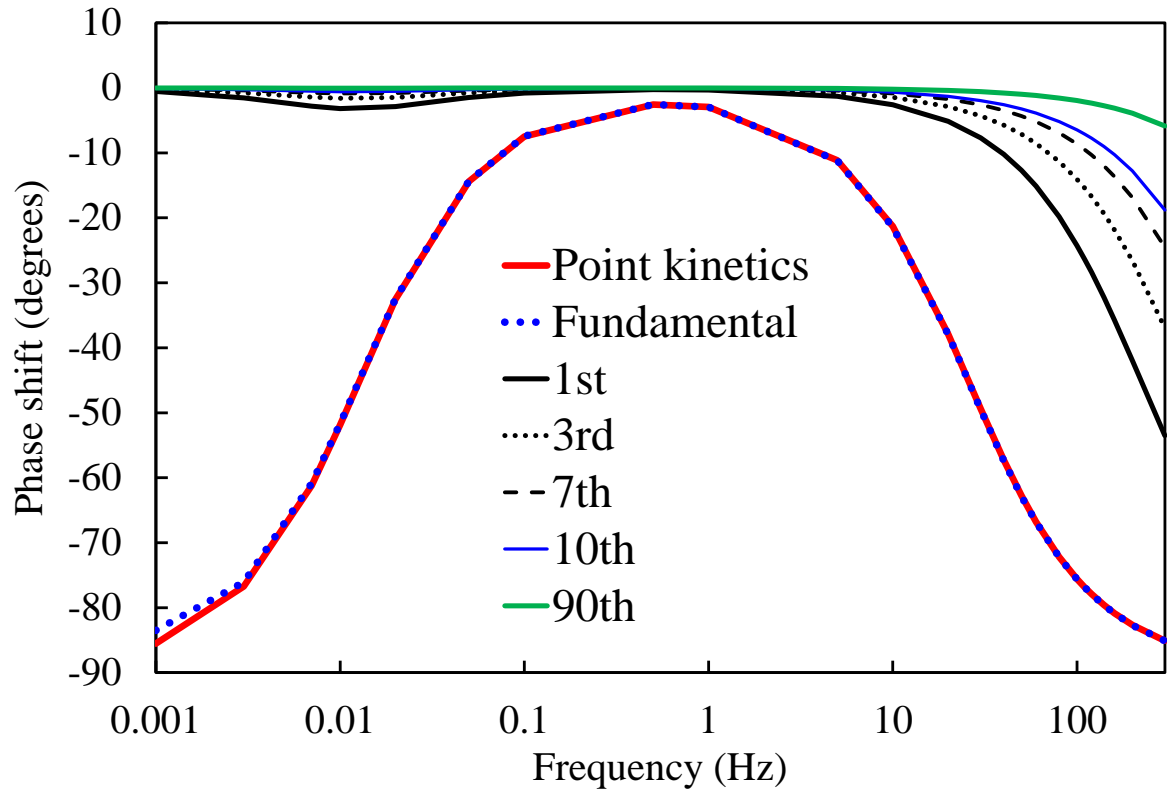
1

2

3   Fig. 6 Frequency dependence of the phase shift of expansion coefficient.
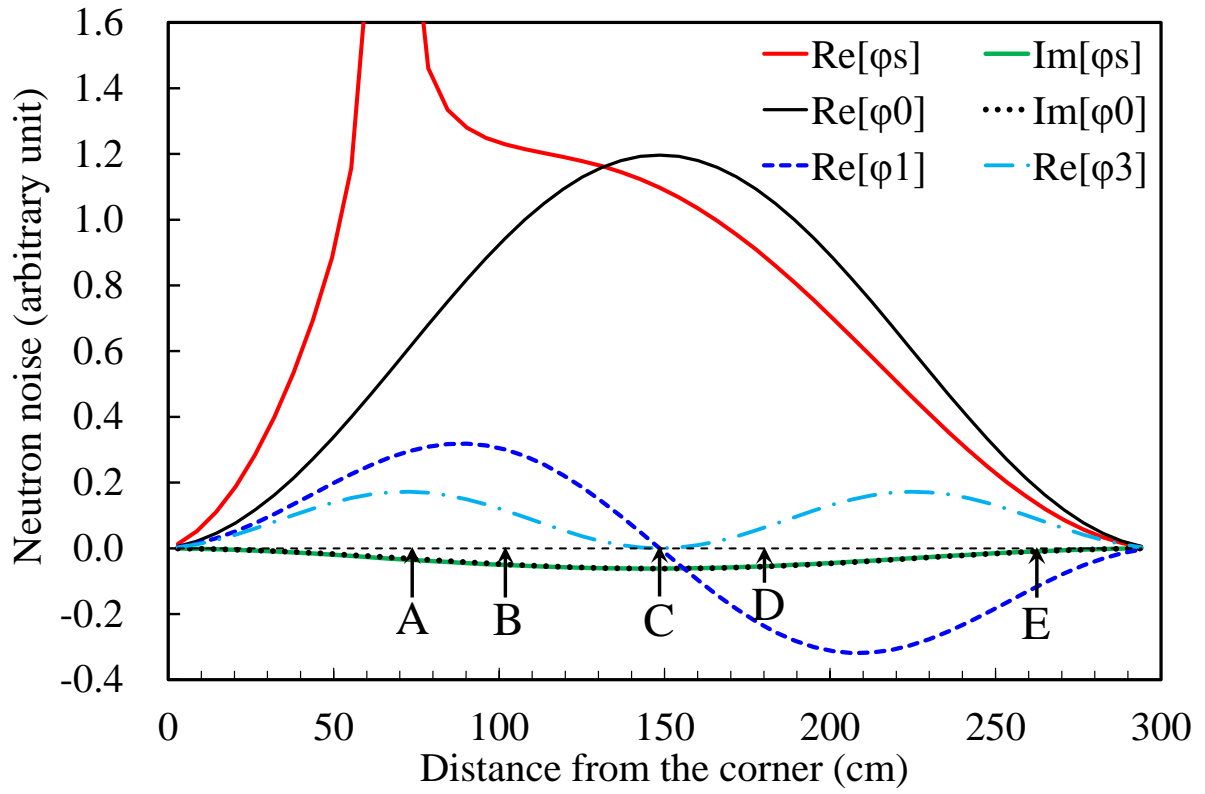
4

Fig. 7 Thermal neutron noise distribution and the decomposed higher-order mode components along the diagonal line (1 Hz).

1

2
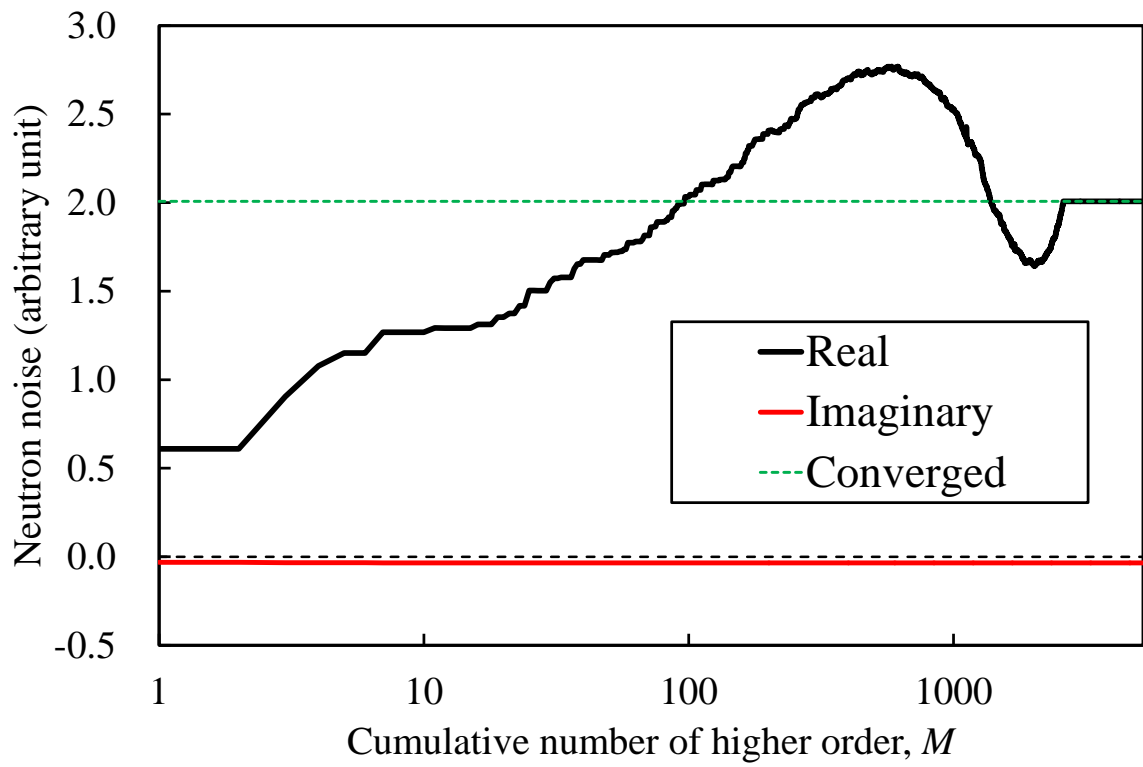
3 Fig. 8 Convergence of the thermal neutron noise at position A (near the noise source, 1 Hz).
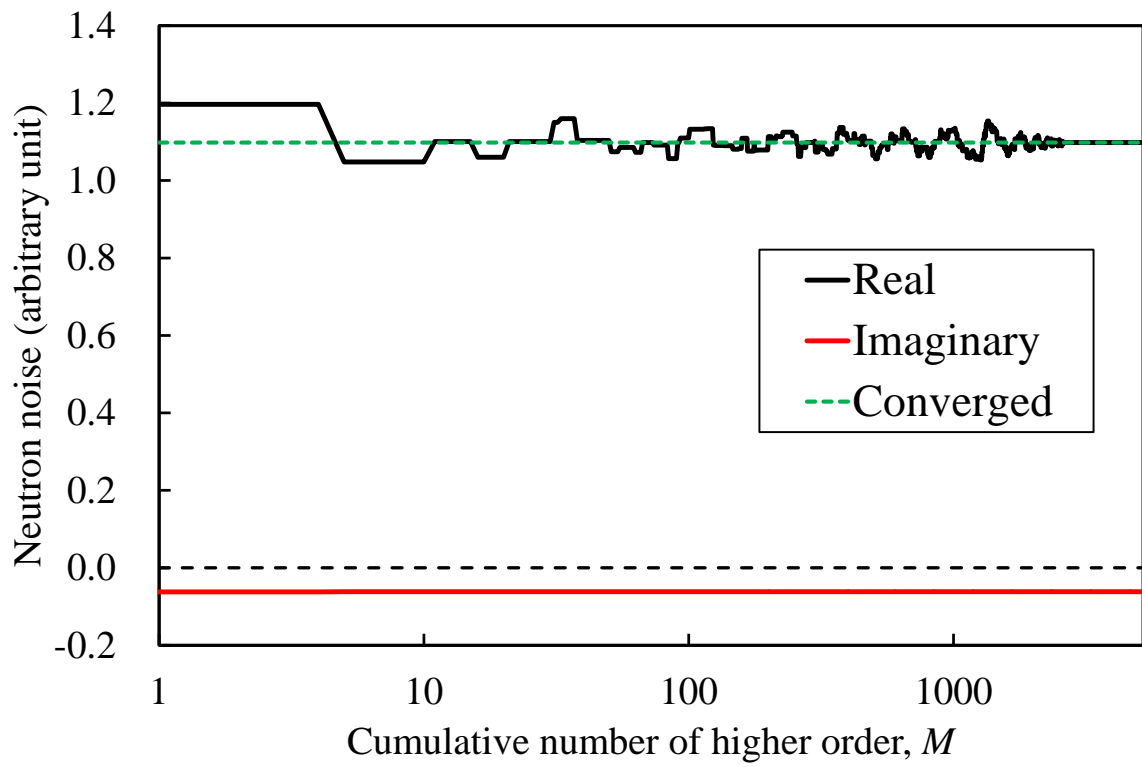
4

Fig. 9 Convergence of the thermal neutron noise at position C (core center, 1 Hz).
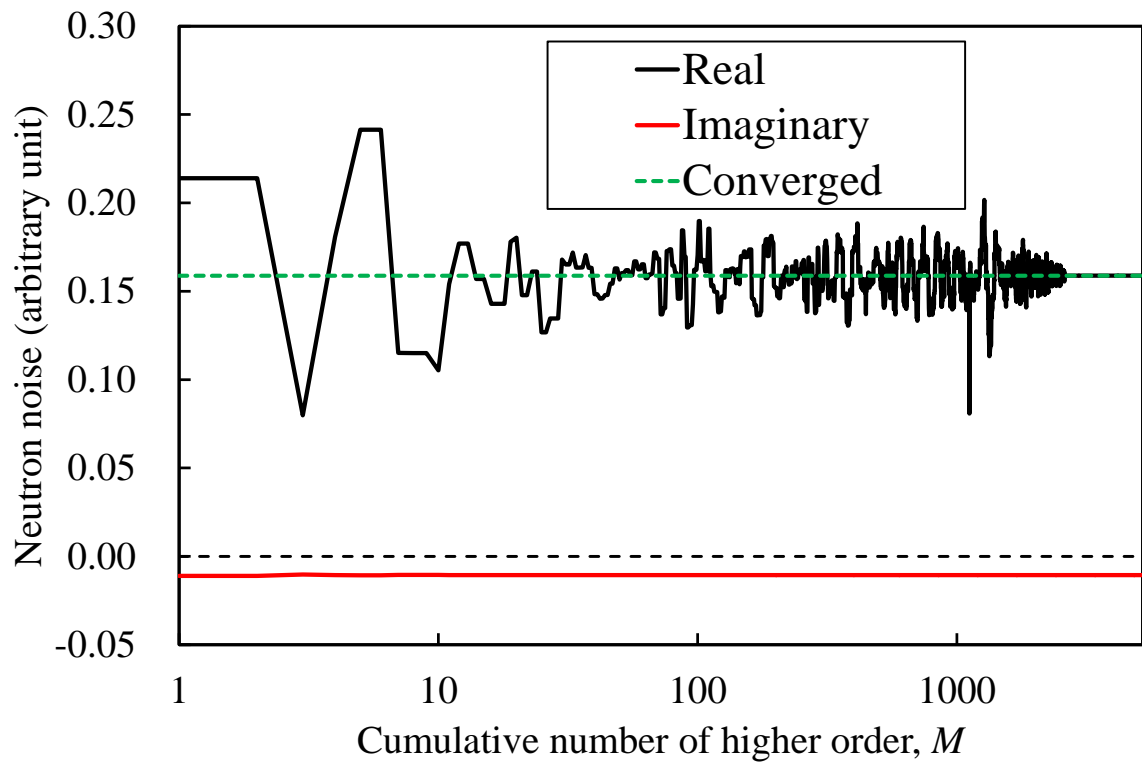
Fig. 10 Convergence of the thermal neutron noise at position E (1 Hz).
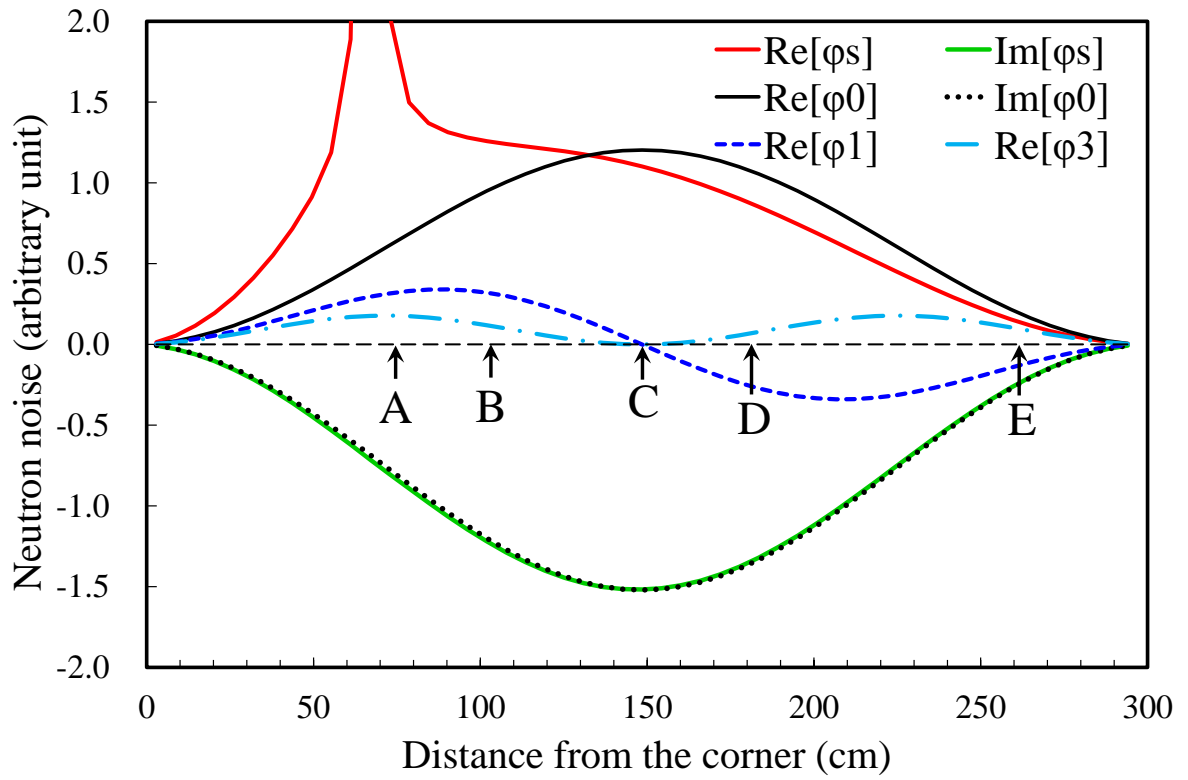
1

2

3 Fig. 11 Thermal neutron noise distribution and the decomposed higher-order mode components

4 along the diagonal line (0.01 Hz).

5

6
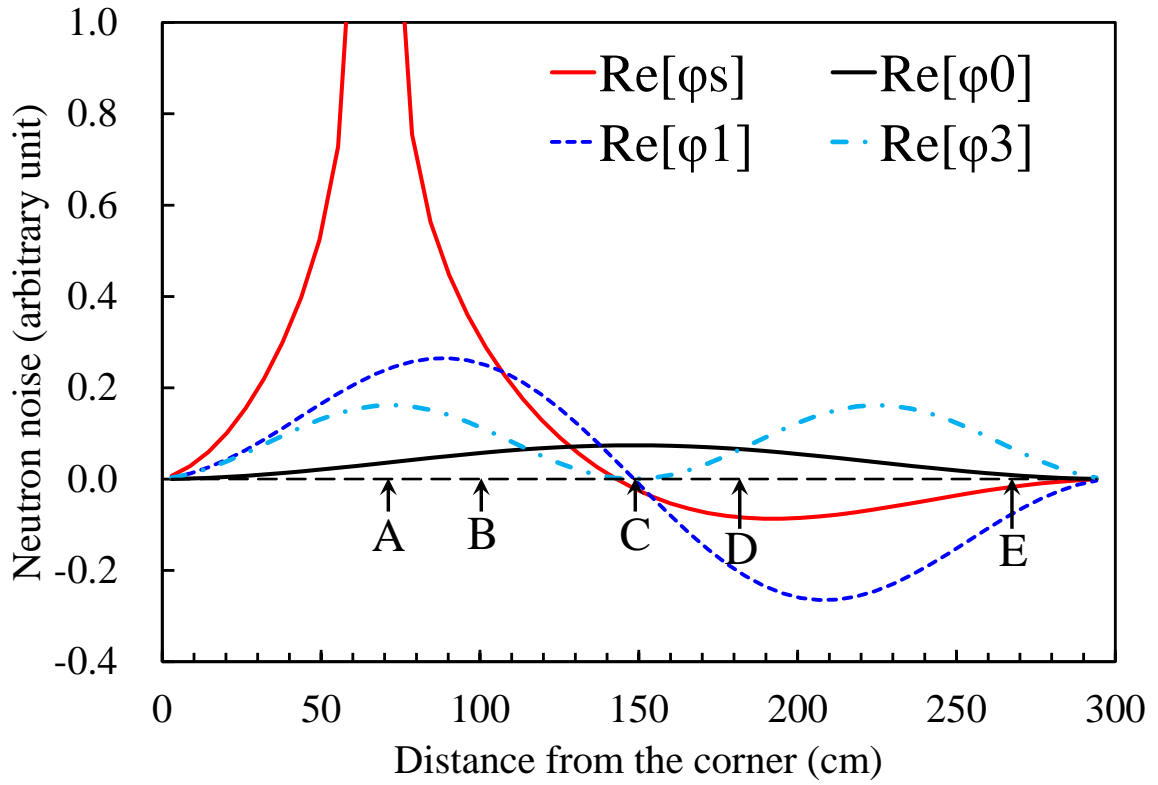
1

2

3 Fig. 12 Thermal neutron noise distribution and the decomposed higher-order mode components

4 along the diagonal line (Real part, 100 Hz).

5

6
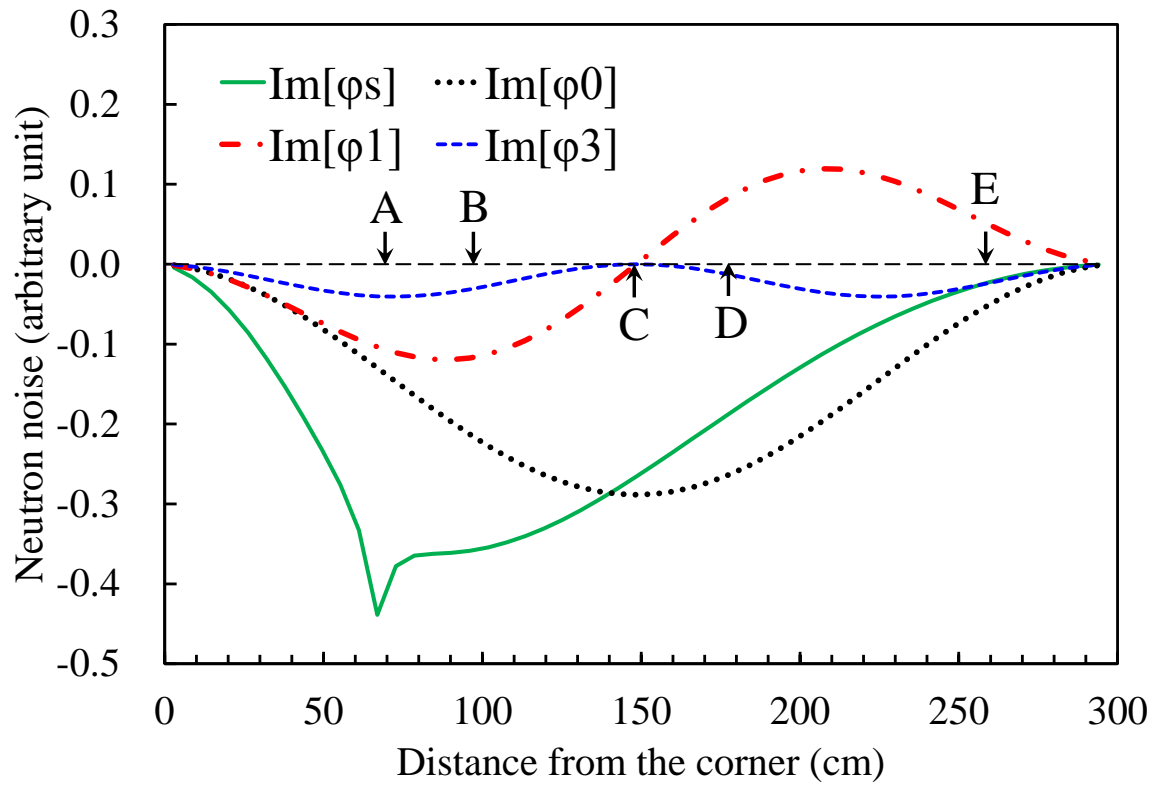
Fig. 13 Thermal neutron noise distribution and the decomposed higher-order mode components along the diagonal line (Imaginary part, 100 Hz).

1

2
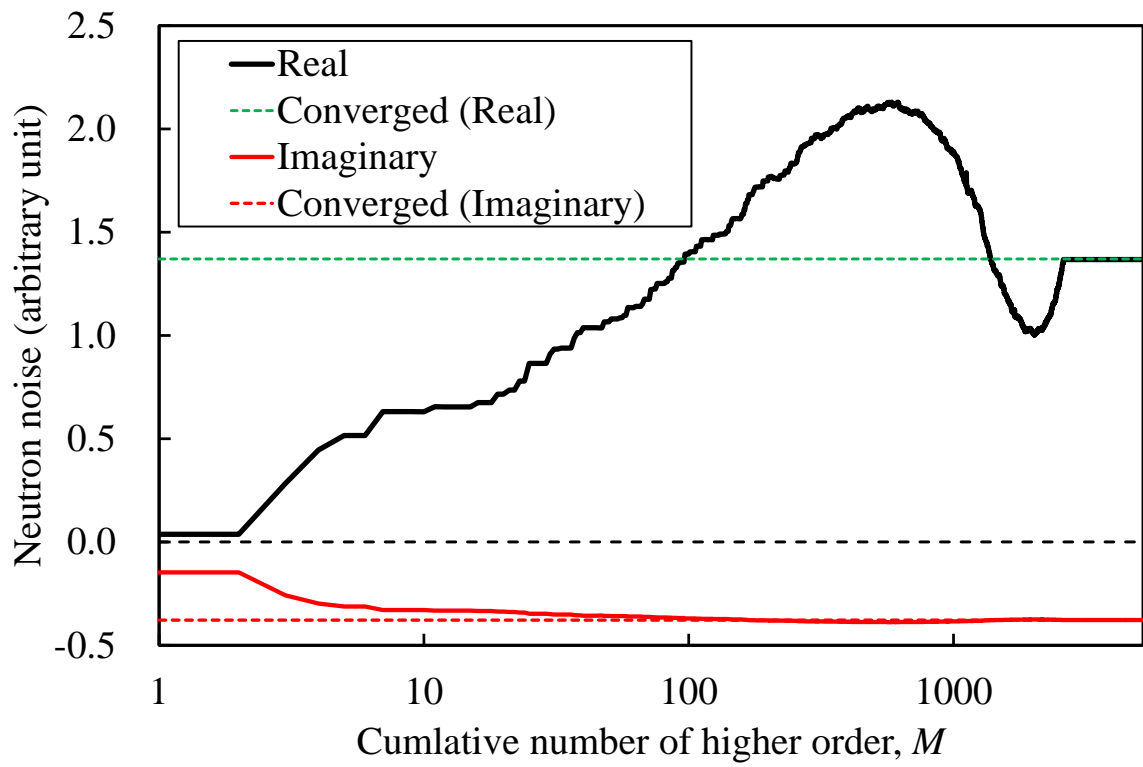
3   Fig. 14 Convergence of the thermal neutron noise at position A (near the noise source, 100 Hz).
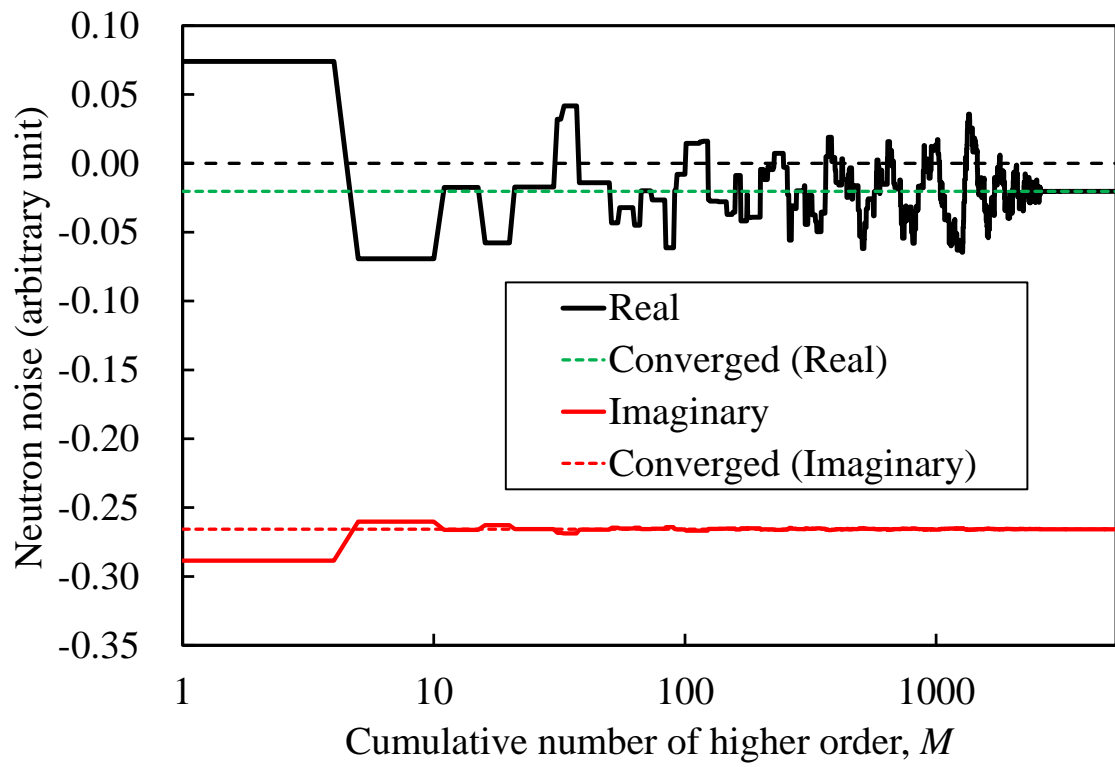
4

5

1

2

3   Fig. 15 Convergence of the thermal neutron noise at position C (core center, 100 Hz).
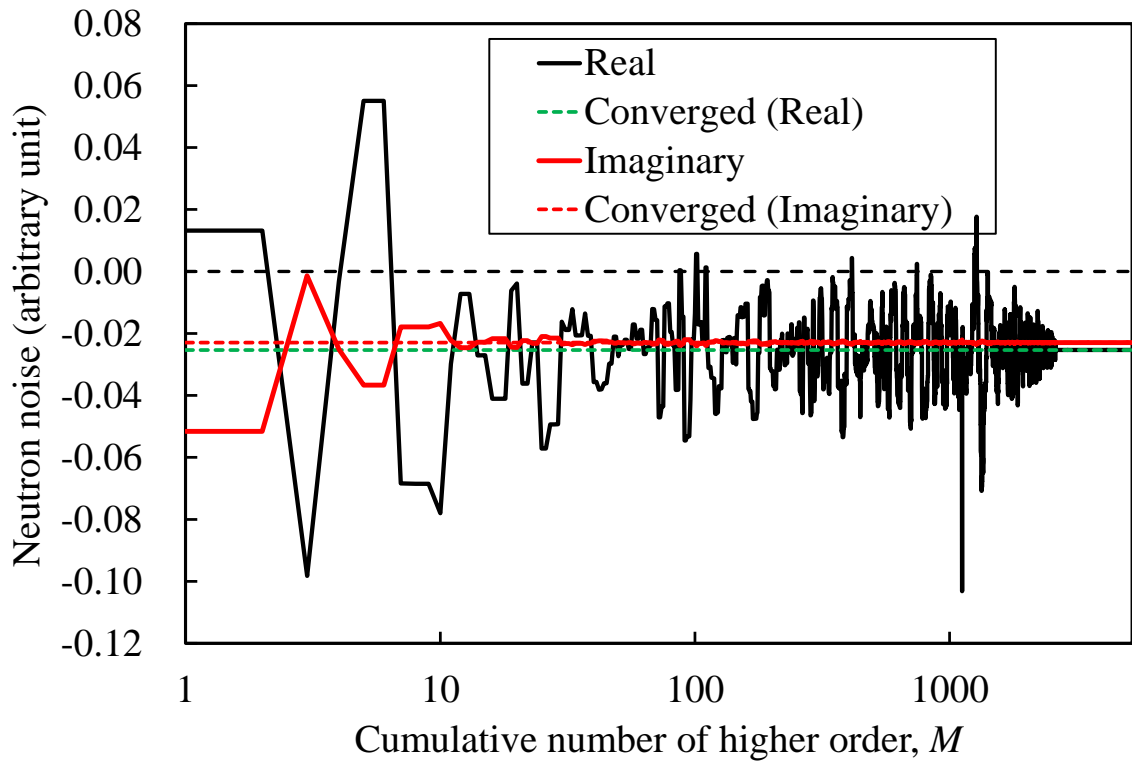
4

5

Fig. 16 Convergence of the thermal neutron noise at position E (100 Hz).

Table

Table 1 Group constants and kinetics parameters

D_1 (cm)	1.709
D_2 (cm)	0.5290
$\nu\Sigma_{f1}$ (cm^{-1})	0.004653
$\nu\Sigma_{f2}$ (cm^{-1})	0.07254
Σ_{a1} (cm^{-1})	0.0067433
Σ_{a2} (cm^{-1})	0.059218
$\Sigma_s^{1\rightarrow2}$ (cm^{-1})	0.01271
v_1 (cm/s)	1.92×10^7
v_2 (cm/s)	3.16×10^5
β	0.007
λ (s^{-1})	0.08